PHYSICAL REVIEW B **109**, 045144 (2024)

Editors' Suggestion

Itinerant ferromagnetism in transition metal dichalcogenide moiré superlattices

Pawel Potasz,[1,*] Nicolás Morales-Durán,[2] Nai Chao Hu,[2] and Allan H. MacDonald[2]
[1]*Institute of Physics, Faculty of Physics, Astronomy and Informatics, Nicolaus Copernicus University, Grudziadzka 5, 87-100 Toruń, Poland*
[2]*Department of Physics, University of Texas at Austin, Austin, Texas 78712, USA*

(Received 26 September 2023; revised 3 January 2024; accepted 5 January 2024; published 23 January 2024)

Moiré materials are artificial crystals formed at van der Waals heterojunctions that have emerged as a highly tunable platform that is able to realize much of the rich quantum physics of electrons in atomic scale solids, and in several cases even new quantum phases of matter. Here we use finite-size exact diagonalization methods to explore the physics of single-band itinerant electron ferromagnetism in semiconductor moiré materials. We predict where ferromagnetism is likely to occur in triangular-lattice moiré systems, and where it is likely to yield the highest Curie temperatures.

DOI: 10.1103/PhysRevB.109.045144

I. INTRODUCTION

Moiré materials have already been established as hosts of Mott [1–3] and topological insulators [4], a rich variety of magnetic states [5–8], and recently even fractional Chern insulators [9,10]. They also provide an alternative platform for studies of itinerant electron ferromagnetism [8,11–13]. Ferromagnets are many-electron ground states that break time-reversal but not translational symmetry, have finite macroscopic magnetization, and are more common in metals than in insulators. Ferromagnetic metals exhibit a rich variety of interesting hysteretic magnetoresistive effects that lie at the heart of spintronics [14] and are valuable for technology. Theoretical studies of metallic ferromagnetism in the context of simple one-band Hubbard models [15–22], although rarely physically realistic, have nevertheless helped provide an understanding of the necessary conditions to stabilize such ground states in crystalline materials. The moiré material case, in which isolated bands are common, offers the opportunity to compare theories of single-band itinerant electron ferromagnetism directly with experiment.

In this paper we use exact diagonalization (ED) methods to explore metallic ferromagnetism in the single-band triangular-lattice moiré materials realized in transition metal dichalcogenide (TMD) heterobilayers [23–26] such as $\mathrm{WSe}_2/\mathrm{MoSe}_2$ and $\mathrm{WSe}_2/\mathrm{WS}_2$. We predict where ferromagnetism is most likely to occur and where ferromagnetic transition temperatures are maximized. The restriction of our study to the case in which a single band is partially occupied and well separated from other bands [27] is motivated by a technical consideration, namely, the need to restrict the dimensions of the many-electron Hilbert spaces studied to manageable sizes.[1] Metallic ferromagnetism is interesting in both single-band and multiband systems. In the multiband case local moments from one subset of bands that supply local Hunds magnetism can combine with large spin stiffnesses supplied by another set of bands that validate simple mean-field descriptions, using density functional theory for true atomic scale materials. In contrast, single-band systems are often more difficult to understand, requiring nonperturbative approaches as the one we take here. Although it seems likely that the highest ferromagnetic transition temperatures that can be realized in moiré systems are in multiband systems[2] we nevertheless anticipate that scientific progress can be achieved by comparisons between theory and experiment across a broad range of band-filling factors and bandwidths in the the single isolated-band regime.

Our paper is organized as follows. In Sec. II we specify the model that we study: a triangular-lattice moiré material model with the Hilbert space truncated to the lowest-energy moiré band and interaction matrix elements calculated exactly. In Sec. III we present our numerical results. We examine three different ferromagnetism indicators that are available from finite-size ED calculations: (i) ground-state spin quantum numbers, (ii) magnon energy estimates from the total-momentum dependence of the low-energy many-body excitation spectrum, and (iii) Lanczos spin-susceptibility calculations. All are consistent with the notion that ferromagnetism occurs when the band-filling factor of the lowest-energy hole miniband is around $\nu \sim \frac{3}{4}$. We estimate that Curie temperatures that can reach $T \sim 10$ K. Finally, in Sec. IV we summarize and discuss our findings, estimating conditions for which the single-band model is realistic. We conclude that the single-band approximation is not applicable at $\nu \sim \frac{3}{4}$ in the TMD moiré materials studied experimentally to date, but that it can be realized by choosing systems with the strongest possible moiré potentials and maximizing background screening of the Coulomb interaction.

---

*Corresponding author: ppotasz@umk.pl

[1] Hilbert space dimensions grow exponentially with the number of retained bands.

[2] The highest critical temperature metallic ferromagnets in atomic scale crystals are after all multiband systems.

II. FINITE-SIZE MOIRÉ MATERIAL MODEL

In this paper we will focus on transition metal dichalcogenide heterobilayer moiré materials [23] in which the topmost valence miniband is energetically isolated, so that holes only populate this band upon doping. Because we are interested mainly in understanding where ferromagnetism has a substantial ordering temperature, we focus on the range of twist angles for which the topmost band is relatively dispersive. The single-particle part of the continuum model Hamiltonian describing these systems is [23]

$$H_0 = -\frac{\hbar^2}{2m^*}\boldsymbol{k}^2 + \Delta(\boldsymbol{r}), \tag{1}$$

$$\Delta(\boldsymbol{r}) = 2V_m \sum_{j=1,3,5} \cos(\boldsymbol{b}_j \cdot \boldsymbol{r} + \psi), \tag{2}$$

where the $\boldsymbol{b}_j$ are members of the first shell of moiré reciprocal lattice vectors and m^*, V_m, and ψ are heterojunction specific parameters. The specific calculations we report on below take effective mass $m^* = 0.35\, m_0$, where m_0 is the rest mass of the electron, moiré modulation strength $V_\text{m} = 25$ meV, and moiré potential shape parameter [24] $\psi = -94^\circ$. These numerical values correspond to $\text{WSe}_2/\text{MoSe}_2$ heterobilayer moirés [23]. It is known [28,29] that strain relaxation of the moiré pattern strengthens the moiré modulation potential, an effect that can be incorporated approximately simply by increasing the value of V_m. For this reason we take a slightly larger value for the moiré modulation than the one reported for the unstrained bilayer [23]. (Approximate scaling relations relating our results to those at larger values of V_m are explained in the Sec. IV.)

Figures 1(a) and 1(b) illustrate the implied moiré band structures and densities of states. The density-of-states maximum occurs at the energy of a saddle-point van Hove singularity (VHS) at band filling $\nu \approx \frac{3}{4}$, where $\nu = \frac{N}{2M}$ with N the number of valence band holes in the system (we call them particles from now on), and M the number of moiré unit cells. We will find that ferromagnetism occurs when the van Hove singularity is close to the Fermi level of the competing paramagnetic state. The position of the van Hove singularity (VHS) shifts slightly to larger band-filling factors ν with increasing twist angle. The VHS is manifested in finite-size calculations with M unit cells by a bunching of discrete states in a small energy interval. In Fig. 1(c) we show the discrete single-particle spectra of (c) $M = 16$ and (d) $M = 36$ meshes. When momentum space is discrete, the thermodynamic limit VHS results in a set of closely spaced discrete energies slightly below $E = 15$ meV. When these states are occupied only by majority spins and all other states are doubly occupied the filling factor is $\nu = 0.72$ for $M = 16$ and $\nu = 0.74$ for $M = 36$ system sizes, respectively. Note that single-particle states at general momenta in the Brillouin-zone interior are sixfold degenerate simply due to triangular-lattice rotational symmetries; this property is responsible for the bunching near $E = 5.0$ meV for $M = 16$ and near $E = 2.5$, 7.0, and 9.0 meV for $M = 36$. [γ point ($\mathbf{k} = 0$) states are nondegenerate and Brillouin zone corner states are doubly degenerate, the degeneracy between K and K' points.] As is commonly recognized, the bunching of single-particle energy levels has an impact on finite-size many-body results, and limits the types of conclusions that can be reached. We will consider a variety of different finite-size geometries, each with a corresponding discretization of the moiré Brillouin zone. In order to correctly capture the VHS physics, we seek meshes that neither under-represent nor over-represent the associated high density of states close to $\nu = 0.75$. In the Supplemental Material (SM) [30] we discuss how we choose finite-size geometries for the calculations discussed in the main text (see also Refs. [31–33] therein).

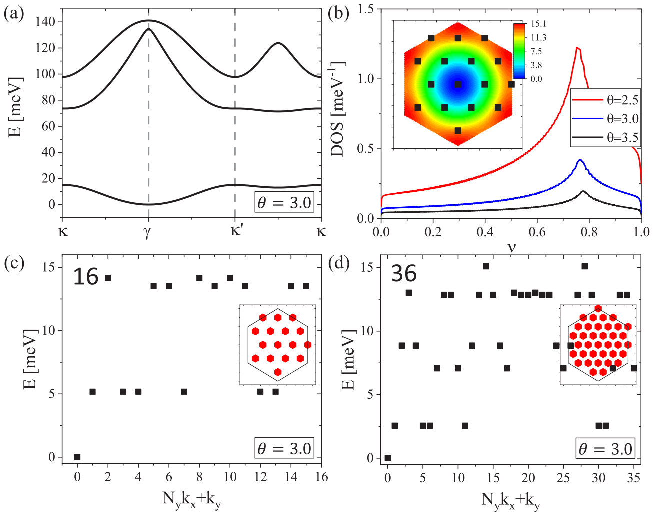

FIG. 1. (a) Particle-hole transformed (hole-picture) band structure of moiré TMD heterobilayers at twist angle $\theta = 3.0$, moiré modulation strength $V_\text{m} = 25$ meV, and shape parameter $\psi = -94^\circ$. Note that the lowest-energy hole miniband is partially occupied and isolated from the remote bands. (b) Density of states (DOS) of the lowest-energy hole miniband vs band filling ν for twist angles $\theta = 2.5,\ 3.0,\ 3.5$. The inset indicates the discrete momenta of a $M = 16$ unit-cell finite-size system within a color scale band contour plot for the $\theta = 3.0$ case. These bands have a van Hove singularity at energy $E_\text{VH} \approx 15$ meV and band-filling factor $\nu_\text{VH} \approx 0.75$ in the thermodynamic limit $M \to \infty$. (c), (d) The discrete energies of the (c) $M = 16$ and (d) $M = 36$ finite-size systems discussed in the text.

The full Hamiltonian is obtained by projecting the two-particle Coulomb interaction term to the topmost valence band shown in Fig. 1(a):

$$\begin{aligned} H &= H_0 + H_\text{I} \\ &= \sum_{\boldsymbol{k},\sigma} \epsilon_{\boldsymbol{k}} c^\dagger_{\boldsymbol{k}\sigma} c_{\boldsymbol{k}\sigma} + \frac{1}{2} \sum_{i,j,k,l\sigma,\sigma'} V^{\sigma,\sigma'}_{i,j,k,l}\ c^\dagger_{\boldsymbol{k}_i\sigma} c^\dagger_{\boldsymbol{k}_j\sigma'} c_{\boldsymbol{k}_l\sigma'} c_{\boldsymbol{k}_k\sigma}, \end{aligned} \tag{3}$$

where $c^\dagger_{\boldsymbol{k}\sigma}$ ($c_{\boldsymbol{k}\sigma}$) creates (annihilates) a particle with momentum $\boldsymbol{k}$ and spin σ, $\epsilon_{\boldsymbol{k}}$ are band energies, and the Coulomb matrix elements are given by

$$V^{\sigma,\sigma'}_{i,j,k,l} = \frac{1}{A} \sum_{\boldsymbol{G}_i,\boldsymbol{G}_j,\boldsymbol{G}_k,\boldsymbol{G}_l}{}^{\prime} \left(z^*_{\boldsymbol{k}_i,\boldsymbol{G}_i} z^*_{\boldsymbol{k}_j,\boldsymbol{G}_j} z_{\boldsymbol{k}_k,\boldsymbol{G}_k} z_{\boldsymbol{k}_l,\boldsymbol{G}_l} \right) \frac{2\pi e^2}{\epsilon\, q}, \tag{4}$$

with $z_{\boldsymbol{k},\boldsymbol{G}}$ eigenstate coefficients obtained from diagonalization of Hamiltonian H_0 given by Eq. (1) in a basis of plane waves $\boldsymbol{G}$. In Eq. (4), A is moiré unit-cell area, momentum conservation implies that matrix elements are nonzero only if $\boldsymbol{k}_i + \boldsymbol{k}_j = \boldsymbol{k}_k + \boldsymbol{k}_l$ modulo a moiré reciprocal lattice vector,

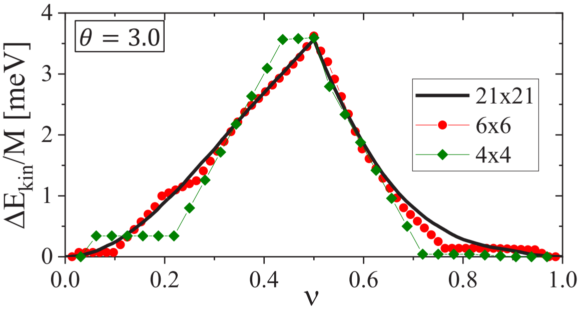

FIG. 2. Kinetic energy difference between maximal and minimal spin-polarized states per moiré cell $\Delta E_{\rm kin}/M = [E_{\rm kin}^{\rm min}(S^z_{\rm max}) - E_{\rm kin}^{\rm min}(S^z_{\rm min})]/M$ as a function of band-filling factor $\nu = N/2M$ for $\theta = 3.0$.

the prime on the sum over the $\mathbf{G}$'s implies that $\boldsymbol{k}_i + \mathbf{G}_i + \boldsymbol{k}_j + \mathbf{G}_j = \boldsymbol{k}_k + \mathbf{G}_k + \boldsymbol{k}_l + \mathbf{G}_l$, and $q = |\boldsymbol{q}| = |\boldsymbol{k}_i + \mathbf{G}_i - \boldsymbol{k}_k - \mathbf{G}_k|$ is the momentum transfer. As we have shown previously [34], by working in a Wannier representation the matrix elements can be reexpressed in terms of a single large parameter, the onsite Coulomb interaction U_0, and a series of smaller parameters including nonlocal exchange, interaction-assisted hopping, and longer-range local interactions. The strength of interactions depends on the value used for the effective dielectric constant ϵ, which represents screening by the three-dimensional dielectric environment of the moiré system. We return to this issue in Sec. IV.

The physics of ferromagnetism is often viewed qualitatively as a competition between band energies, which favor states with minimal spin-polarization and interaction energies, which favor spin-polarized states because many-electron wave functions must vanish when electrons with parallel spins approach each other, thereby avoiding strong repulsive interactions. The gain in interaction energy per unit cell is often referred to as the Stoner energy I. In Fig. 2 we compare finite-size kinetic energies for single Slater-determinant (SD) states with maximal and minimal spin polarization in triangular-lattice moiré materials $\Delta E_{\rm kin} = E_{\rm kin}^{\rm min}(S^z_{\rm max}) - E_{\rm kin}^{\rm min}(S^z_{\rm min})$, where the superscripts "min" emphasize that the occupation numbers are chosen to minimize the kinetic energy subject to the spin-polarization constraint. The energy difference per moiré period reaches its maximum when the band is half-filled because this is the filling factor with the maximum possible spin polarization per moiré cell. The kinetic energy cost increases with twist angle θ because of increasing bandwidths (see SM [30]). Note that the kinetic energy cost of spin alignment is, for the most part, reasonably well approximated at relatively small system sizes, and that the kinetic energy cost is very small for large band-filling factors because of the VHS near the top of the first hole miniband. This is the filling-factor regime where itinerant ferromagnetism might be expected.

III. EXACT DIAGONALIZATION RESULTS

We will discuss three different indicators for ferromagnetism that are available from finite-size calculations. First of all we consider the total spin quantum number of the finite-size many-electron ground state. The absence of spin-orbit coupling in our model allows a ferromagnet to be defined as a system in which the ground-state total spin quantum number S is extensive. We find that maximal spin polarization is common in finite-size systems at band-filling factors larger than about $\frac{3}{4}$, and conclude that ferromagnetism will occur through much of this filling-factor range. In the following subsections we estimate the temperature to which ferromagnetism survives in two different ways: (i) by extracting magnon energies from the momentum dependence of the many-body excitation spectrum and (ii) by extracting finite-temperature Stoner energies I from the temperature-dependent spin susceptibilities calculated using finite-temperature Lanczos methods.

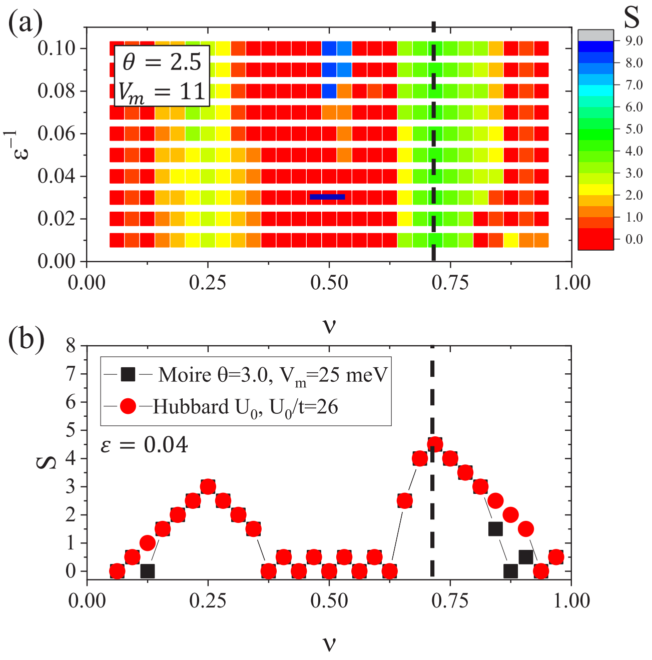

FIG. 3. The ground-state total spin S as a function of filling factor ν from exact diagonalization calculations for a system with $M = N_1 \times N_2 = 16$ unit cells (N_1 and N_2 are defined in SM [30]). (a) Spin-polarization map: total spin as a function of filling factor ν and dielectric constant ϵ for twist angle $\theta = 2.5$ and moiré potential strength $V_{\rm m} = 11$ meV. A horizontal blue line labels the metal-insulator transition at half-filling [35]. (b) Comparison of the ground-state spin polarization of the moiré continuum Hamiltonian and the corresponding on-site Hubbard model for dielectric constant $\epsilon^{-1} = 0.04$, twist angle $\theta = 3.0$, moiré strength $V_{\rm m} = 25$ meV, and moiré shape $\psi = -94°$. A dashed line indicates the position of the van Hove singularity for finite-size mesh.

A. Ground-state spin

We first assess the tendency toward ferromagnetism by comparing ground-state energies in different total spin S sectors. Typical results are summarized in Fig. 3(a), where we plot ground-state spin quantum numbers vs ν and the interaction strength parameter ϵ^{-1}. Large ground-state spins appear in several different regimes in this plot. First of all they appear at small band-filling factors and weak interactions.

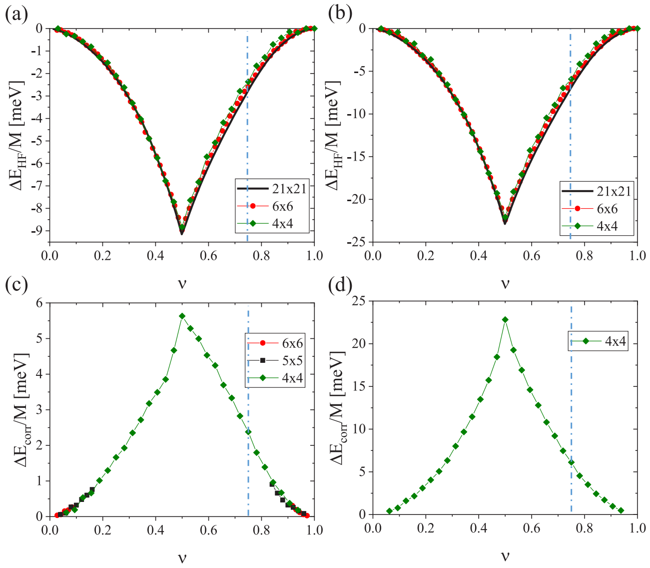

FIG. 4. Exchange energy and correlation energy difference between maximally $S_{\rm max}$ and minimally $S_{\rm min}$ spin-polarized states normalized per moiré unit cell. These plots are based on finite-size ED calculations for $M = 16$ and on non-self-consistent Hartree-Fock, single Slater determinant (SD), for $M = 441$. A dashed line indicates the position of the van Hove singularity. (a), (c) For interaction strength $\epsilon^{-1} = 0.04$ and (b), (d) for interaction strength $\epsilon^{-1} = 0.1$. These plots are for twist angle $\theta = 3.0$, moiré modulation strength $V_{\rm m} = 25$ meV, and potential shape $\psi = -94^\circ$.

We view ferromagnetism in this regime as an artifact of the symmetry-related momentum-space shell degeneracy of the finite-size mesh used to produce these results, which we have illustrated in Fig. 1. Second, ferromagnetism is seen near half-filling of the band at large interaction strengths. The ground state at $\nu = \frac{1}{2}$ for this range of interaction parameters is an interaction-induced insulator [the blue line in Fig. 3(a) labels a metal-insulator transition estimated from the charge-gap calculations using a definition $\Delta_C = E_{\rm tot}(N+1) + E_{\rm tot}(N-1) - 2E_{\rm tot}(N)$ (see also Ref. [23]], but the ground state is ferromagnetic rather than antiferromagnetic because spatially indirect exchange interactions ($\propto \epsilon^{-1}$) exceed antiferromagnetic superexchange interactions ($\propto \epsilon$). The property that Mott insulators are sometimes ferromagnetic in moiré materials has been discussed previously [34]. Our main interest here is in the very robust ferromagnetic states that appear near band filling $\nu = \frac{3}{4}$, where the ground state is metallic. In Fig. 3(b) we plot the ground-state spin vs ν in the moderate interaction strength regime, where nonlocal exchange is unimportant, demonstrating that its value is unchanged when the interaction model is truncated to include only the onsite Hubbard-type Coulomb interaction term. In the SM [30] we show that the magnetic competition in the insulating state at $\nu = \frac{1}{2}$ is shifted in favor of antiferromagnetism with increasing twist angle, as expected since larger bandwidths imply stronger superexchange interactions.

In Fig. 4 we analyze the competition between ferromagnetism and paramagnetism by partitioning the total energy into four different contributions: kinetic energy $E_{\rm kin}$, Hartree energy $E_{\rm H}$, Fock (exchange) energy $E_{\rm exch}$, and correlation energy $E_{\rm corr}$. Convergence to the thermodynamic limit is easily obtained for the first three terms, whereas the fourth part, the correlation energy, must be estimated from finite-size calculations and extrapolated to the thermodynamic limit. For the purposes of the qualitative point that we wish to make in this paragraph, we define the sum of the first three terms as the expectation value of the full Hamiltonian in the single Slater-determinant (SD) state constructed by occupying the lowest-energy single-particle states for a given spin polarization. We define the mean-field interaction energy difference $\Delta E_{\rm HF} = \Delta E_{\rm H} + \Delta E_{\rm exch}$ between maximally and minimally spin-polarized SD states by subtracting the kinetic energy contribution to the energy difference:

$$\Delta E_{\rm HF} = \Delta E_{\rm SD} - \Delta E_{\rm kin}. \tag{5}$$

Note that $\Delta E_{\rm HF}$ accounts for the fact that the shape of the charge distribution within the unit cell is different in the spin-polarized and unpolarized states, an effect that is absent in the Hubbard model. Because of this effect, the lowest-energy SD state is not always the one constructed from the lowest-energy single-particle states. In the SM [30] we show results for $\Delta E_{\rm exch}$ obtained from multiband self-consistent Hartree-Fock calculations. These energies have larger negative values because of the additional band-mixing degrees of freedom that are optimized.

The correlation energy is defined as the difference between the ED ground-state energy and the lowest-energy SD ground-state energy in a given spin sector with subtracted kinetic energies contributions

$$\begin{aligned} E_{\rm corr}(S_{\rm max}) = {} & E_{\rm tot}(S_{\rm max}) - E^{\rm kin}_{\rm tot}(S_{\rm max}) \\ & - \big[E_{\rm SD}(S_{\rm max}) - E^{\rm kin}_{\rm SD}(S_{\rm max})\big]. \end{aligned} \tag{6}$$

Here we used the following definitions:

$$\begin{aligned} E_{\rm tot}(S) &= \langle \Psi_{\rm GS}(S)|H_0 + H_{\rm I}|\Psi_{\rm GS}(S)\rangle, \\ E^{\rm kin}_{\rm tot}(S) &= \langle \Psi_{\rm GS}(S)|H_0|\Psi_{\rm GS}(S)\rangle, \\ E_{\rm SD}(S) &= \langle \Phi_{\rm GS}(S)|H_0 + H_{\rm I}|\Phi_{\rm GS}(S)\rangle, \\ E^{\rm kin}_{\rm SD}(S) &= \langle \Phi_{\rm GS}(S)|H_0|\Phi_{\rm GS}(S)\rangle, \end{aligned}$$

where $|\Psi_{\rm GS}(S)\rangle$ is ED ground-state wave function in a total spin sector S and $|\Phi_{\rm GS}(S)\rangle = \prod_{\mathbf{k}\sigma} c^\dagger_{\mathbf{k}\sigma}|0\rangle$ is lowest-energy SD state. The correlation energy difference is

$$\Delta E_{\rm corr} = E_{\rm corr}(S_{\rm max}) - E_{\rm corr}(S_{\rm min}). \tag{7}$$

With the above definitions, the total-energy difference is

$$\Delta E_{\rm tot} = \Delta E_{\rm SD} + \Delta E_{\rm corr}. \tag{8}$$

In Fig. 4 we see that mean-field interaction energies $\Delta E_{\rm HF}$ strongly favor spin-polarized states, and that the degree to which interactions favor spin-polarized states is strongly reduced when correlations are included. For the parameters of this calculation, increasing the strength of interactions actually does not substantially increase the degree to which interactions favor spin polarization. This is precisely the problem in estimating where ferromagnetism occurs; once correlations are strong, electrons avoid each other well even if they have the same spin, and even in metallic states. Ferromagnetism is most likely when one subset of states has a

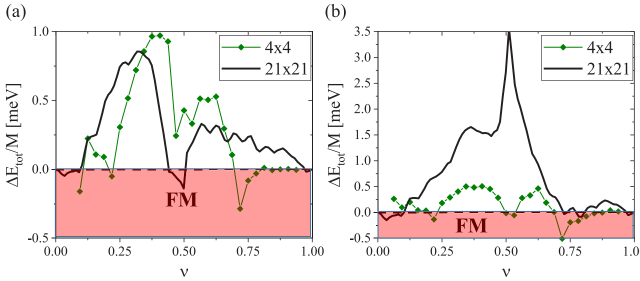

FIG. 5. The total-energy difference between maximally $S_{\max}$ and minimally $S_{\min}$ spin-polarized states $\Delta E_{\text{tot}} = E_{\text{tot}}(S_{\max}) - E_{\text{tot}}(S_{\min})$ per moiré unit cell for (a) $\epsilon^{-1} = 0.04$ and for (b) $\epsilon^{-1} = 0.1$. ΔE_{tot} for $M = 16$ is obtained from ED calculations and for $M = 441$ from exchange energy and extrapolated correlation energy from ED. These results were obtained with model parameters $\theta = 3.0$, $V_{\text{m}} = 25$ meV, and $\psi = -94°$.

high density of states so that it is easily polarized, and the remaining states are strongly dispersive so that correlations are suppressed. Conditions favorable for ferromagnetism are regularly achieved in multiband systems, like the paradigmatic late 3d transition metals. In single-band systems somewhat less favorable conditions can be achieved by having a sharp maximum in the density of states. For two-dimensional (2D) materials, maxima always appear at saddle points in the band structure. It follows that single-band ferromagnetism in 2D moiré materials is most likely when the Fermi level of the paramagnetic state is close to a saddle point in the band structure.

A typical result for the competition in total energy between fully spin-polarized and depolarized states is summarized in Fig. 5 where we see that ferromagnetism is most likely near $\nu = \frac{3}{4}$ as expected. The Hartree-Fock theory results for the weaker of the two interaction strengths considered tell a cautionary tale about finite-size effects since they predict ferromagnetism for $M = 16$ finite-size systems and paramagnetism for $M = 441$ finite-size systems; the $M = 16$ mesh overstates the van Hove singularity (see Fig. 2). In a vicinity of half-filling ferromagnetism is predicted for $M = 441$ but the energy of SD state with $S = S_{\min}$ is not the lowest one here; instead, a state with broken translation symmetry, the three sublattice Néel state, is expected to have lower energy and competes with FM; both of these two states have been indeed observed in experiment [1,6]. For stronger interactions, ferromagnetism is predicted in a vicinity of $\nu = 0.75$ for both meshes. In the following sections, we focus on estimates of transition temperatures for ferromagnetism around this particular filling, indicated by a black dashed line in Fig. 3.

B. Magnon energies

In metallic ferromagnets with large splitting between majority-spin and minority-spin quasiparticle energies, the ordering temperature is typically limited by collective thermal fluctuations. The Curie temperature then scales with the energies of the magnon modes, just as it does in insulating magnets. In Fig. 6(a) we show the spin-flip excitation spectrum of a typical maximally spin-polarized state near $\nu = \frac{3}{4}$. We associate the 15 lowest-energy excitations (one for each nonzero momentum) with magnon modes and the higher-energy excitations with unbound quasiparticle spin-flip excitations. We see that the magnon energies are several times smaller than the quasiparticle spin-splitting energy. In Fig. 6(b) we show the twist angle dependence of the highest magnon energy, which grows with the bandwidth, suggesting that spin stiffness is supplied mainly by band dispersion.

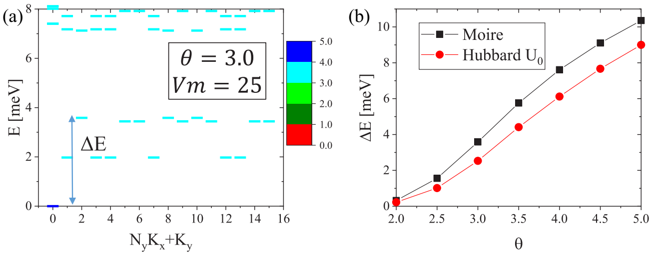

FIG. 6. Spin-flip excitation spectrum of a $M = N_{\text{x}} \times N_{\text{y}} = 16$ fully polarized ground state. (a) Energy spectrum for total spin $S = S_{\max} - 1$ for the system with $N_{\text{h}} = 9$ holes ($N = 23$, $\nu = 0.73$), corresponding to the filling factor ν indicated by a dashed line in Fig. 3, $\epsilon^{-1} = 0.04$, $\psi = -94°$. The 16 lowest-energy excitations can be associated with magnon collective modes, and the higher-energy excitations with unbound spin-flip particle-hole excitations. ΔE indicates the width of the magnon spectrum, which scales with the transition temperature. N_{x} (N_{y}) is the number of unit cells along two directions determined by real-space lattice vectors $\mathbf{a}_1$ and $\mathbf{a}_2$ on a triangular lattice, K_{x} (K_{y}) are total momenta along two directions determined by reciprocal space lattice vectors $\mathbf{b}_1$ and $\mathbf{b}_2$. (b) The width of magnon spectrum ΔE as a function of a twist angle θ for the moiré superlattice and its corresponding Hubbard model.

Since we neglect spin-orbit interactions, our two-dimensional model is spin-rotationally invariant and its critical temperature therefore vanishes (see the effect of spin-orbit interactions on a critical temperature in the SM [30]). We defer to a separate study the issue of engineering strong spin-orbit interactions in TMD triangular-lattice moiré materials in order to suppress long-wavelength thermal fluctuations. Figure 6(b) suggests that ferromagnetic critical temperatures approaching 100 K could be achievable at large twist angles for sufficiently strong spin-orbit interactions. However, it is important to realize that the single-band approximation could fail at large twist angles. We return to this point again in Sec. IV.

C. Finite-temperature Lanczos method

One of the interesting aspects of moiré materials physics from a fundamental point of view is that the regime in which the temperature is comparable to or larger than the bandwidth is experimentally accessible. In the following paragraphs we address the temperature dependence of magnetic properties over this wide energy interval.

For the evaluation of thermodynamic properties in the canonical ensemble, we need to calculate thermal expectation values of relevant operators A:

$$\langle A \rangle = \frac{\sum_{n=1}^{N_{\text{st}}} \langle n | e^{-\beta H} A | n \rangle}{\sum_{n=1}^{N_{\text{st}}} \langle n | e^{-\beta H} | n \rangle}, \tag{9}$$

where $\beta = 1/k_B T$ with k_B the Boltzman constant, the partition function $Z = \sum_{n=1}^{N_{\rm st}} \langle n|e^{-\beta H}|n\rangle$, and $|n\rangle$ is summed over orthonormal basis states. The exponential increase of $N_{\rm st}$ with system size places severe limits on the direct application of these fundamental formulas.

The problem can be avoided if an appropriate statistical average of the full Hilbert space is generated. In the finite-temperature Lanczos method (FTLM) [36] one starts with the high-temperature expansion:

$$\langle A\rangle_{\beta\to 0} = Z^{-1} \sum_{n=1}^{N_{\rm st}} \sum_{k=0}^{\infty} \frac{(-\beta)^k}{k!} \langle n|H^k A|n\rangle, \tag{10}$$

where

$$Z = \sum_{n=1}^{N_{\rm st}} \sum_{k=0}^{\infty} \frac{(-\beta)^k}{k!} \langle n|H^k|n\rangle. \tag{11}$$

The Lanczos algorithm is an iterative method for finding extreme eigenvalue of a large matrix in which expectations of high powers of the Hamiltonian naturally appear. During Lanczos iteration steps, a set of orthogonal basis vectors is generated (a Krylov space), spanning a finite-size space that contains approximations to eigenvectors corresponding to extreme eigenvalues of a full Hilbert space with accuracy controlled by the number of iteration steps. In the Lanczos method the Hamiltonian is diagonalized in this Krylov space obtaining Lanczos eigenvectors $|l\rangle$ and the associated Lanczos energy eigenvalues ϵ_l. When the number of Lanczos steps $N_l \geqslant k$ one can write

$$\begin{aligned}\langle n|H^k A|n\rangle &\approx \sum_{l=0}^{N_L} \langle n|H^k|l(n)\rangle\langle l(n)|A|n\rangle \\ &= \sum_{l=0}^{N_L} (\epsilon_{l(n)})^k \langle n|l(n)\rangle\langle l(n)|A|n\rangle \end{aligned} \tag{12}$$

and

$$\langle n|H^k|n\rangle \approx \sum_{l=0}^{N_L} (\epsilon_{l(n)})^k |\langle l(n)|n\rangle|^2. \tag{13}$$

N_L is a parameter of the approximation that needs to be large enough to reach accurate extremal energy eigenvalues; for the calculations we present below we take $N_L = 150$. Inserting Eqs. (12) and (13) into (10) and (11) and replacing the sum over all orthonormal basis states by a much smaller sum over R random Lanczos seed states, in analogy to Monte Carlo methods, yields

$$\langle A\rangle \approx Z^{-1} \frac{N_{\rm st}}{N_{\rm R}} \sum_{\nu\in N_{\rm R}} \sum_{l}^{N_L} e^{-\beta\epsilon_{l(\nu)}} \langle l(\nu)|A|\nu\rangle\langle \nu|l(\nu)\rangle, \tag{14}$$

where the partition function is

$$Z \approx \frac{N_{\rm st}}{N_{\rm R}} \sum_{\nu}^{N_{\rm R}} \sum_{l}^{N_L} e^{-\beta\epsilon_{l(\nu)}} |\langle l(\nu)|\nu\rangle|^2. \tag{15}$$

The exponential-size Hilbert space of the Hamiltonian is thereby approximated by its spectral representation in a Krylov space spanned by the $N_{\rm L}$ Lanczos vectors starting from each random vector. The chosen random vectors $|\nu\rangle$ should ideally be mutually orthogonal, but for practical purposes this is not really necessary since two vectors with random components in a large dimensional space are always nearly orthogonal.

In general, calculations using this approach are less sensitive to finite-size effects as temperature increases, and most sensitive to finite size at $T = 0$. This property is related to the fact that at $T = 0$ both static and dynamical quantities are calculated from one eigenstate only, and the selection of this state can be dependent on the size and on the shape of the finite-size system. $T > 0$ introduces thermodynamic averaging over a larger number of eigenstates and this directly reduces finite-size effects for static quantities. Calculational efficiency can be improved by taking symmetries into account, so that $N_{\rm st}$ corresponds to the number of states with a given symmetry.

In our view, the finite-temperature Lanczos method (FTLM) is ideally suited to exploring the high-temperature physics that is observable in moiré materials. In this work we focus on calculations of the spin magnetic susceptibilty $\chi = \beta\langle S_z^2\rangle$ where

$$\langle S_z^2\rangle = \frac{\sum_n \exp(-\beta\epsilon_n) S_z(n)^2}{\sum_n \exp(-\beta\epsilon_n)}. \tag{16}$$

Beacuse $[H, S_z] = 0$, the Lanczos method can be applied to each S_z sector separately. The FTLM formula for the susceptibility is

$$\chi = Z^{-1}\beta \sum_s \frac{N_{\rm st}(s)}{N_{\rm R}(s)} \sum_{\nu=1}^{N_{\rm R}(s)} \sum_{l=1}^{N_L} e^{-\beta\epsilon_{l(\nu)}} |\langle l(\nu)|\nu\rangle|^2 s^2, \tag{17}$$

where s is the S_z value for the subspace. We find that the most accurate results are obtained for $N_{\rm R}(s)$ chosen such that the ratio between the Hilbert subspace size and the number of vectors is kept constant.

The accuracy of FTLM finite-size calculations is assessed in Fig. 7 by comparing χ as calculated by performing the full sum over all states with the FTLM sum. The three plots in Fig. 7 [(a) χ/β as a function of inverse temperature β, (b) the susceptibility $\chi(T)$, and the (c) inverse susceptibility $\chi^{-1}(T)$ as a function of temperature T] emphasize different aspects of the temperature dependence of χ. The $\beta \to 0$ ($T \to \infty$) and $\beta \to \infty$ ($T \to 0$) limits of χ/β can be calculated analytically by averaging S_z^2 over the full Hilbert space [$\chi^{-1}/\beta \to M\nu(1-\nu)/2$ for $\beta \to 0$] and over the ground-state spin multiplet [$\chi^{-1}/\beta \to S(S+1)/3$ for $\beta \to \infty$], respectively. For the test case ($M = 16$ and $N = 4$) illustrated in Fig. 7, the susceptibility can be calculated exactly from the full many-body spectrum because the Hilbert space dimension for a given S_z subspace does not exceed 1000. The exact result is indicated by a red line in Fig. 7, and compared with FTLM estimates based on different numbers of random vectors $N_{\rm R}$. All lines overlap for temperatures $T > 20$ K, demonstrating the high accuracy of the method in the high-temperature limit. The ground state of the system in this case has $S = 0$ (see the inset), which leads to vanishing susceptibility in (b) and divergence of the inverse susceptibility in (c) as $T \to 0$. The susceptibility reaches a maximum at around $T = 4$ K. The blue line in (c) is a high-temperature linear fit that extrapolates

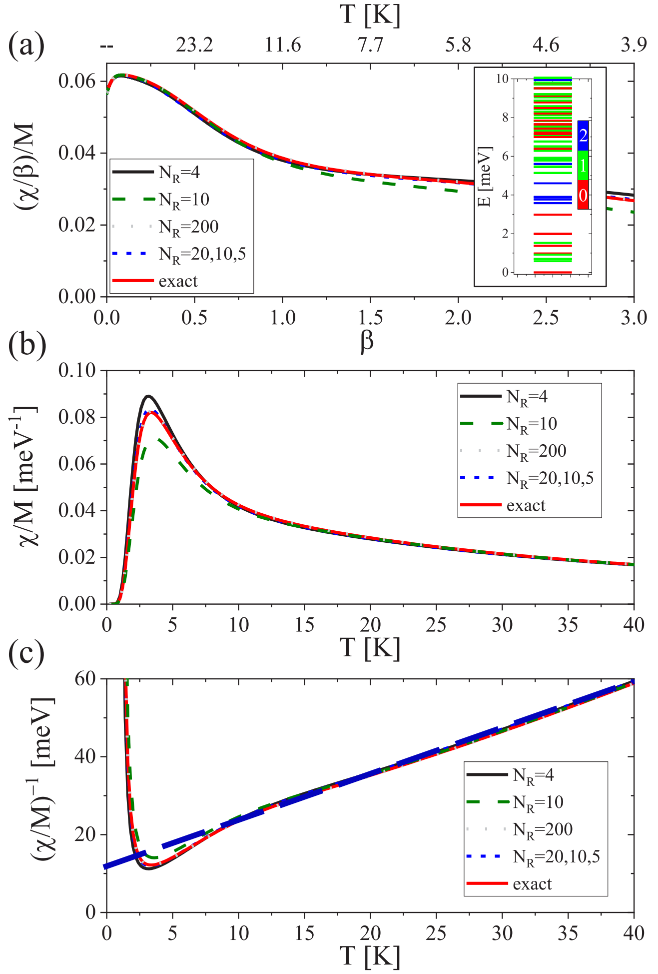

FIG. 7. Comparison of FTLM and exact susceptibility calculations for $M = 16$ moiré unit cells, $N = 4$ electrons, and different number of random vectors N_R. (a) χ/β as a function of inverse temperature β. The inset shows low-energy many-body spectrum with total spin indicated by color. (b) Susceptibility $\chi(T)$ and (c) inverse susceptibility $\chi^{-1}(T)$ as a function of temperature T. The blue line in (c) is a linear fit to estimate a transition temperature T_C. The number of Lanczos steps is taken to be $N_L = 150$. The size of the Hilbert space for $S_z = 0$ and fixed total momentum **K** is weakly momentum dependent and around 900. The parameters for this illustration are interaction strength $\epsilon^{-1} = 0.04$, twist angle $\theta = 3.0$, $V_m = 25$ meV, and $\psi = -94°$. $N_R = 20, 10, 5$ means that for $S_z = 0$ we take $N_R = 20$, $S_z = \pm 1$ we take $N_R = 10$, and so on. If one number is given, for all subspaces we take the same N_R.

to a finite value for $T = 0$, consistent with a paramagnetic state.

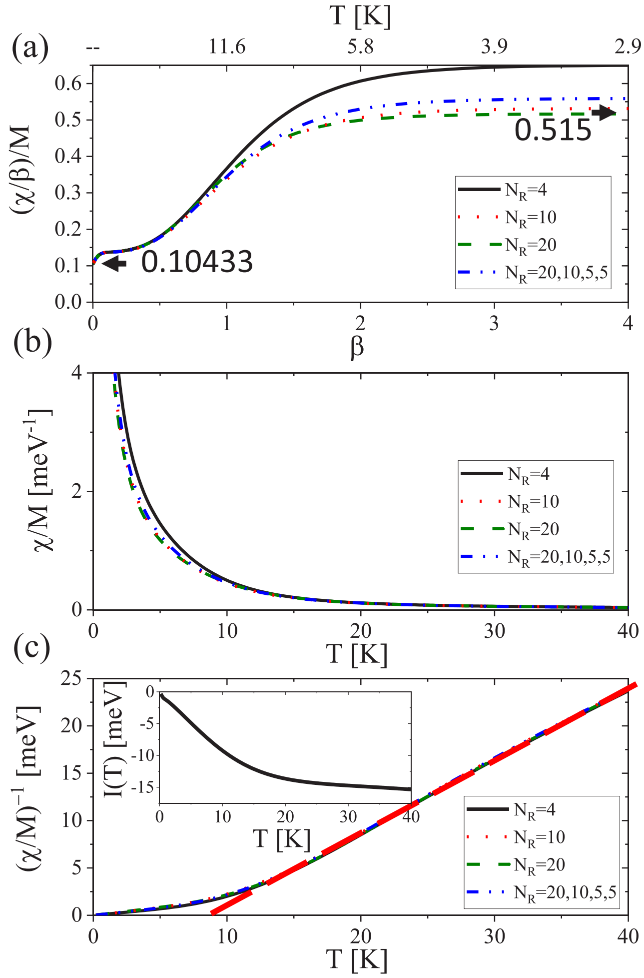

FIG. 8. FTLM susceptibility calculations for $M = 16$ moiré unit cells, $N = 23$ electrons (9 holes), and different number of random vectors N_R. (a) χ/β normalized per moiré cell as a function of inverse temperature β. Analytically calculated values are given for the limit of infinite temperature (left) and zero temperature (right). (b) Susceptibility $\chi(T)$ and (c) inverse susceptibility $\chi^{-1}(T)$ as a function of temperature T. The red line is a linear fit to estimate the transition temperature T_C. The inset shows the Stoner parameter $I(T) \equiv \chi^{-1}(T)/M - \chi_{\rm NI}^{-1}(T)/M$, where NI means noninteracting. The number of Lanczos steps was $N_L = 150$. The size of Hilbert space for $S_z = 0$ at fixed total momentum **K** is around 5×10^5. $N_R = 20, 10, 5, 5$ means that for $S_z = \pm 0.5$ we take $N_R = 20$, $S_z = \pm 1.5$ we take $N_R = 10$, and for all other subspaces $N_R = 5$. If one number is given, for all subspaces we take the same N_R. The parameters used for this calculation are dielectric constant $\epsilon^{-1} = 0.04$, twist angle $\theta = 3.0$, $V_m = 25$ meV, and $\psi = -94°$.

The FTLM estimates have the advantage that they can be drawn from larger Hilbert spaces. In Fig. 8 we show a typical result obtained for $N = 23$ particles ($N_h = 9$ holes) in the $M = 16$ case, in the regime of filling factors where ferromagnetism is expected on the basis of the many-body ground-state calculations. In this case the many-body ground state has nonzero total spin $S = \frac{9}{2}$. The exact value of $\chi/M\beta$ normalized per moiré unit cell in the $\beta \to \infty$ limit is therefore 0.515, as indicated by a black arrow in Fig. 8(a). (The $\beta \to 0$ limit 0.104 33, which is independent of interactions, is also indicated by a black arrow.) We see that the FTLM method gives accurate results in both limits, irrespective of N_R at $T \to \infty$ and for $N_R \geqslant 10$ at $T = 0$. Generally speaking, the ratio between N_R and the dimension of a given Hilbert subspace is a good accuracy indicator. The increase in χ at intermediate temperatures relative to the high-temperature limit shows that on average interactions lower the energies of states with larger S_z relative to those with smaller S_z. The linear fit to the inverse susceptibility shown in Fig. 8(c) estimates the Curie temperature $T_C \approx 9$ K for this case, and the estimate is not strongly affected by N_{R} in reasonable ranges. The inset shows the finite-size Stoner parameter I that has the expected linear-in-T dependence up to around $T \approx 12$ K.

Having established the efficacy of the FTLM, we now employ it to study trends in ferromagnetism in triangular-lattice moiré materials. In the SM [30] in Figs. S2(b) and S2(d) we compare inverse susceptibility results for two other twist angles for the same moiré modulation potential. Extrapolating from high temperatures where finite-size effects are less severe, we see that the susceptibility at higher temperatures decreases with twist angle. We attribute this decrease to an increase in bandwidth, which decreases the Pauli susceptibility of noninteracting electrons. At the same time, the high-temperature estimate of the Curie temperature at which the susceptibility diverges (the inverse susceptibility vanishes) increases with twist angle. We attribute this increase also to increasing bandwidth, which increases magnon energies by increasing the kinetic energy cost of spatial modulation of the magnetization.

IV. DISCUSSION

We have used three different indicators available from finite-size exact diagonalization calculations to address the physics of itinerant ferromagnetism in single-band triangular-lattice moiré materials: (i) ground-state spin quantum numbers, (ii) magnon excitation energies, and (iii) temperature-dependent spin susceptibilities. All indicate that ferromagnetism is common at hole band-filling factors near $\nu = \frac{3}{4}$ at temperatures up to $\sim$10 K. Our calculations were performed for particular values of the moiré modulation strength and shape parameters. These are, however, expected to be strongly dependent on the specific heterojunction at which the moiré pattern is formed, and in particular on strain relaxations at those heterojunctions which will tend to increase modulation strengths [28,29]. When $V_m \rightarrow \lambda V_m$, twist angle $\theta \rightarrow \sqrt{\lambda}\theta$, and dielectric screening parameter $\epsilon \rightarrow \sqrt{\lambda}\epsilon$, the three terms in the continuum model Hamiltonian (interaction, moiré potential, and kinetic energy) all increase by a factor of λ. Since the properties of interest here are relatively insensitive to the interaction strength parameter within reasonable ranges, it follows that the properties of systems with stronger moiré potentials can be read off from our results by increasing temperature scales and twist angles. In particular, the larger energy scales increase the temperatures at which ferromagnetism can occur.

It is interesting to compare TMD triangular-lattice moiré materials, with graphene multilayer moiré materials that also support ferromagnetic states. In the latter case, it is known that because of topological obstructions inherited from the individual layer Dirac cones [37–39], a faithful representation of the flat moiré minibands requires multiband tight-binding [40] models, for which the exact diagonalization approach is not practical. In the TMD moiré material case, however, the lowest-energy moiré bands have Wannier functions that are similar to harmonic oscillator ground states centered on moiré potential extrema [23]. Although we do not approximate the interaction matrix elements in our one-band model, we have verified that all properties related to ferromagnetism are similar to those of simple triangular-lattice Hubbard models.

It is also interesting to compare TMD triangular-lattice materials with rhombohedral graphene multilayers [41–49], a class of two-dimensional materials in which metallic ferromagnetism has been discovered recently. These graphene multilayer systems are like TMD moiré materials in that they have peaks in their densities of states, related in that case to Liftshitz transitions of distorted Dirac cones, but they do not have minibands and are not approximated by Hubbard models. The magnetism that appears in these systems is consistent with the notion that the key to ferromagnetism is a sharp density-of-states peak in a low-density-of-states background.

At the mean-field level, the critical temperature of the ferromagnetic state is proportional to the exchange splitting Δ_{exch} between majority- and minority-spin bands. The classic metallic ferromagnets, like cobalt, iron, or nickel, are well known to have transition temperatures T_{c} that are much lower than the exchange splitting Δ_{exch}. Measured critical temperatures are more comparable to typical magnon energies E_{mag} ($k_B T_{\mathrm{c}} \sim E_{\mathrm{mag}} \ll \Delta_{\mathrm{exch}}$). Critical temperature estimates based on fermionic mean-field approximation do not work well for itinerant ferromagnets, actually in agreement with our results. We believe that our Hubbard model systems are, in this sense, in the same regime as the classical $3d$ ferromagnets.

The exact diagonalization method we have employed is most suitable when the many-electron Hilbert space can be truncated to a single moiré miniband. The small parameter which controls the applicability of this approximation is the ratio of the largest interaction scale, the onsite Hubbard interaction U_0, to the subband separation. As explained in Ref. [23] these can be estimated by making a harmonic approximation for the moiré potential. We find that $U_0 \sim \mathrm{Ry}^{3/4}(zV_m)^{1/4}(a_B/a_M)^{1/2}$, where $z = 6$ is the triangular-lattice coordination number and Ry and a_B are the host 2D semiconductor Rydberg energy scale $\sim$0.3 eV and Bohr radius length scale $\sim$1 nm. Similarly, the subband separation $\hbar\omega \sim \mathrm{Ry}^{1/2}(zV_m)^{1/2}a_B/a_M$. It follows that

$$\frac{U_0}{\hbar\omega} \sim (\mathrm{Ry}/zV_m)^{1/4}(a_M/a_B)^{1/2}. \tag{18}$$

Truncation to the lowest moiré band is justified at all band-filling factors $\nu \in (0, 1)$ when the right-hand side of Eq. (18) is smaller than $\sim$1. Most systems [50,51] that have been studied to date do not satisfy this criterion. Since continuum model approximations are valid only for $a_M \gtrsim a_B$, it follows that single-band ferromagnetism will occur only when the first factor on the right side of Eq. (18) is made small, for example by increasing the dielectric screening environment of the moiré system to decrease Ry, or by choosing a system with a particularly large value of V_m. From exponentially localized Wannier functions obtained for the topmost valence band used in our calculations, we get, for $\theta = 3.0$, $U_0\epsilon \approx 1121$ meV [34], $\hbar\omega \approx 58.5$ meV. For $\epsilon^{-1} = 0.1$, $\frac{U_0(\epsilon^{-1}=0.1)}{\hbar\omega} > 1$, while for $\frac{U_0(\epsilon^{-1}=0.04)}{\hbar\omega} < 1$. Thus, for the limit of weaker interaction strength the single-band approximation is justified. This suggests that our predictions are relevant for systems with sufficiently close nearby gates.

We note that Coulomb repulsion will increase the energy of the lowest-energy hole miniband, as it is filled, by more than it increases the energies of states in higher-energy moiré minibands. For this reason the regime of parameter space in which occupation of higher-energy minibands can be neglected decreases as band-filling factor increases. When correlations are included, the ground state at hole-filling factor $\nu = \frac{1}{2}$ is often an insulator. When its lowest-energy hole-charged excitation is dominantly in a higher-hole miniband, the insulator is referred to as a charge transfer insulator [50,51]. Since single-band ferromagnetism is most likely near band-filling factor $\nu = \frac{3}{4}$, the present single-band study is never relevant when the ground state of the half-filled band is a charge transfer insulator, which already involves higher-energy subbands in an essential way. If systems could be realized in which the sign of V_m is reversed (or equivalently $\psi \rightarrow \psi + 180^\circ$), ferromagnetism would be expected for minibands that are less than half-filled. For the standard sign of V_m, however, any ferromagnetism that occurs when the interaction parameter that is the subject of Eq. (18) is large, must be of multiband character. We leave the analysis of this situation for a future study, for it requires a different approach.

ACKNOWLEDGMENTS

The authors acknowledge helpful interactions with L. Fu and Y. Zhang. This work was supported by the U.S. Department of Energy, Office of Science, Basic Energy Sciences, under Award No. DE-SC0022106. P.P. acknowledges support from the Polish National Science Centre based on Decision No. 2021/41/B/ST3/03322. We acknowledge the Texas Advanced Computing Center (TACC) at The University of Texas at Austin for providing high-performance computer resources.

[1] Y. Tang, L. Li, T. Li, Y. Xu, S. Liu, K. Barmak, K. Watanabe, T. Taniguchi, A. H. MacDonald, J. Shan, and K. F. Mak, Simulation of Hubbard model physics in WSe_2/WS_2 moiré superlattices, Nature (London) **579**, 353 (2020).

[2] T. Li, S. Jiang, L. Li, Y. Zhang, K. Kang, J. Zhu, K. Watanabe, T. Taniguchi, D. Chowdhury, L. Fu, J. Shan, and K. F. Mak, Continuous Mott transition in semiconductor moiré superlattices, Nature (London) **597**, 350 (2021).

[3] A. Ghiotto, E.-M. Shih, G. S. S. G. Pereira, D. A. Rhodes, B. Kim, J. Zang, A. J. Millis, K. Watanabe, T. Taniguchi, J. C. Hone, L. Wang, C. R. Dean, and A. N. Pasupathy, Quantum criticality in twisted transition metal dichalcogenides, Nature (London) **597**, 345 (2021).

[4] T. Li, S. Jiang, B. Shen, Y. Zhang, L. Li, Z. Tao, T. Devakul, K. Watanabe, T. Taniguchi, L. Fu, J. Shan, and K. F. Mak, Quantum anomalous Hall effect from intertwined moiré bands, Nature (London) **600**, 641 (2021).

[5] Y. Tang, K. Su, L. Li, Y. Xu, S. Liu, K. Watanabe, T. Taniguchi, J. Hone, C.-M. Jian, C. Xu, K. F. Mak, and J. Shan, Evidence of frustrated magnetic interactions in a Wigner–Mott insulator, Nat. Nanotechnol. **18**, 233 (2023).

[6] E. Anderson, F.-R. Fan, J. Cai, W. Holtzmann, T. Taniguchi, K. Watanabe, D. Xiao, W. Yao, and X. Xu, Programming correlated magnetic states with gate-controlled moiré geometry, Science **381**, 325 (2023).

[7] L. Ciorciaro, T. Smoleński, I. Morera, N. Kiper, S. Hiestand, M. Kroner, Y. Zhang, K. Watanabe, T. Taniguchi, E. Demler, and A. İmamoğlu, Kinetic magnetism in triangular moiré materials, Nature **623**, 509 (2023).

[8] Z. Tao, W. Zhao, B. Shen, P. Knüppel, K. Watanabe, T. Taniguchi, J. Shan, and K. F. Mak, Observation of spin polarons in a frustrated moiré Hubbard system, arXiv:2307.12205.

[9] J. Cai, E. Anderson, C. Wang, X. Zhang, X. Liu, W. Holtzmann, Y. Zhang, F. Fan, T. Taniguchi, K. Watanabe, Y. Ran, T. Cao, L. Fu, D. Xiao, W. Yao, and X. Xu, Signatures of fractional quantum anomalous Hall states in twisted $MoTe_2$, Nature (London) **622**, 63 (2023).

[10] Y. Zeng, Z. Xia, K. Kang, J. Zhu, P. Knüppel, C. Vaswani, K. Watanabe, T. Taniguchi, K. F. Mak, and J. Shan, Thermodynamic evidence of fractional chern insulator in moiré $MoTe_2$, Nature (London) **622**, 69 (2023).

[11] H. Jia, B. Ma, R. L. Luo, and G. Chen, Double exchange, itinerant ferromagnetism, and topological Hall effect in moiré heterobilayer, Phys. Rev. Res. **5**, L042033 (2023).

[12] M. Davydova, Y. Zhang, and L. Fu, Itinerant spin polaron and metallic ferromagnetism in semiconductor moiré superlattices, Phys. Rev. B **107**, 224420 (2023).

[13] K. Lee, P. Sharma, O. Vafek, and H. J. Changlani, Triangular lattice Hubbard model physics at intermediate temperatures, Phys. Rev. B **107**, 235105 (2023).

[14] S. D. Bader and S. Parkin, Spintronics, Annu. Rev. Condens. Matter Phys. **1**, 71 (2010).

[15] H. Tasaki, From Nagaoka's ferromagnetism to Flat-Band ferromagnetism and beyond: An introduction to ferromagnetism in the Hubbard model, Prog. Theor. Phys. **99**, 489 (1998).

[16] T. Hanisch, G. S. Uhrig, and E. Müller-Hartmann, Lattice dependence of saturated ferromagnetism in the Hubbard model, Phys. Rev. B **56**, 13960 (1997).

[17] K. Held and D. Vollhardt, Microscopic conditions favoring itinerant ferromagnetism: Hund's rule coupling and orbital degeneracy, Eur. Phys. J. B **5**, 473 (1998).

[18] T. Obermeier, T. Pruschke, and J. Keller, Ferromagnetism in the large-u Hubbard model, Phys. Rev. B **56**, R8479 (1997).

[19] Y. Kamogawa, J. Nasu, and A. Koga, Ferromagnetic instability for the single-band Hubbard model in the strong-coupling regime, Phys. Rev. B **99**, 235107 (2019).

[20] M. Lebrat, M. Xu, L. H. Kendrick, A. Kale, Y. Gang, P. Seetharaman, I. Morera, E. Khatami, E. Demler, and M. Greiner, Observation of Nagaoka polarons in a Fermi-Hubbard quantum simulator, arXiv:2308.12269.

[21] M. L. Prichard, B. M. Spar, I. Morera, E. Demler, Z. Z. Yan, and W. S. Bakr, Directly imaging spin polarons in a kinetically frustrated Hubbard system, arXiv:2308.12951.

[22] I. Morera, M. Kanász-Nagy, T. Smolenski, L. Ciorciaro, A. Imamoğlu, and E. Demler, High-temperature kinetic magnetism in triangular lattices, Phys. Rev. Res. **5**, L022048 (2023).

[23] F. Wu, T. Lovorn, E. Tutuc, and A. H. MacDonald, Hubbard model physics in transition metal dichalcogenide moiré bands, Phys. Rev. Lett. **121**, 026402 (2018).

[24] H. Pan, F. Wu, and S. Das Sarma, Band topology, Hubbard model, Heisenberg model, and Dzyaloshinskii-Moriya interaction in twisted bilayer wse$_2$, Phys. Rev. Res. **2**, 033087 (2020).

[25] E. Y. Andrei, D. K. Efetov, P. Jarillo-Herrero, A. H. MacDonald, K. F. Mak, T. Senthil, E. Tutuc, A. Yazdani, and A. F. Young, The marvels of moiré materials, Nat. Rev. Mater. **6**, 201 (2021).

[26] D. M. Kennes, M. Claassen, L. Xian, A. Georges, A. J. Millis, J. Hone, C. R. Dean, D. N. Basov, A. N. Pasupathy, and A. Rubio, Moiré heterostructures as a condensed-matter quantum simulator, Nat. Phys. **17**, 155 (2021).

[27] N. Morales-Durán, P. Potasz, and A. H. MacDonald, Magnetism and quantum melting in moiré-material Wigner crystals, Phys. Rev. B **107**, 235131 (2023).

[28] S. Shabani, D. Halbertal, W. Wu, M. Chen, S. Liu, J. Hone, W. Yao, D. N. Basov, X. Zhu, and A. N. Pasupathy, Deep moiré potentials in twisted transition metal dichalcogenide bilayers, Nat. Phys. **17**, 720 (2021).

[29] C. Wang, X.-W. Zhang, X. Liu, Y. He, X. Xu, Y. Ran, T. Cao, and D. Xiao, Fractional chern insulator in twisted bilayer MoTe$_2$, arXiv:2304.11864.

[30] See Supplemental Material at http://link.aps.org/supplemental/10.1103/PhysRevB.109.045144 for the results for different twist angles, momentum space meshes, a detail comparison between moiré continuum model and Hubbard model, and the role of spin-orbit coupling on the transition temperature estimation.

[31] J. Oitmaa and D. D. Betts, The ground state of two quantum models of magnetism, Can. J. Phys. **56**, 897 (1978).

[32] A. Avella and F. Mancini, *Strongly Correlated Systems* (Springer, Berlin, 2013).

[33] C. Repellin, B. A. Bernevig, and N. Regnault, $\mathbb{Z}_2$ fractional topological insulators in two dimensions, Phys. Rev. B **90**, 245401 (2014).

[34] N. Morales-Durán, N. C. Hu, P. Potasz, and A. H. MacDonald, Nonlocal interactions in moiré Hubbard systems, Phys. Rev. Lett. **128**, 217202 (2022).

[35] N. Morales-Durán, A. H. MacDonald, and P. Potasz, Metal-insulator transition in transition metal dichalcogenide heterobilayer moiré superlattices, Phys. Rev. B **103**, L241110 (2021).

[36] J. Jaklič and P. Prelovšek, Lanczos method for the calculation of finite-temperature quantities in correlated systems, Phys. Rev. B **49**, 5065 (1994).

[37] L. Zou, H. C. Po, A. Vishwanath, and T. Senthil, Band structure of twisted bilayer graphene: Emergent symmetries, commensurate approximants, and Wannier obstructions, Phys. Rev. B **98**, 085435 (2018).

[38] Z. Song, Z. Wang, W. Shi, G. Li, C. Fang, and B. A. Bernevig, All magic angles in twisted bilayer graphene are topological, Phys. Rev. Lett. **123**, 036401 (2019).

[39] H. C. Po, L. Zou, T. Senthil, and A. Vishwanath, Faithful tight-binding models and fragile topology of magic-angle bilayer graphene, Phys. Rev. B **99**, 195455 (2019).

[40] Z.-D. Song and B. A. Bernevig, Magic-angle twisted bilayer graphene as a topological heavy Fermion problem, Phys. Rev. Lett. **129**, 047601 (2022).

[41] H. Zhou, L. Holleis, Y. Saito, L. Cohen, W. Huynh, C. L. Patterson, F. Yang, T. Taniguchi, K. Watanabe, and A. F. Young, Isospin magnetism and spin-polarized superconductivity in bernal bilayer graphene, Science **375**, 774(R) (2022).

[42] H. Zhou, T. Xie, A. Ghazaryan, T. Holder, J. R. Ehrets, E. M. Spanton, T. Taniguchi, K. Watanabe, E. Berg, M. Serbyn, and A. F. Young, Half- and quarter-metals in rhombohedral trilayer graphene, Nature (London) **598**, 429 (2021).

[43] H. Zhou, T. Xie, T. Taniguchi, K. Watanabe, and A. F. Young, Superconductivity in rhombohedral trilayer graphene, Nature (London) **598**, 434 (2021).

[44] C. Huang, T. M. R. Wolf, W. Qin, N. Wei, I. V. Blinov, and A. H. MacDonald, Spin and orbital metallic magnetism in rhombohedral trilayer graphene, Phys. Rev. B **107**, L121405 (2023).

[45] Y. Lee, S. Che, J. Velasco Jr., X. Gao, Y. Shi, D. Tran, J. Baima, F. Mauri, M. Calandra, M. Bockrath, and C. N. Lau, Gate-tunable magnetism and giant magnetoresistance in suspended rhombohedral-stacked few-layer graphene, Nano Lett. **22**, 5094 (2022).

[46] A. M. Seiler, F. R. Geisenhof, F. Winterer, K. Watanabe, T. Taniguchi, T. Xu, F. Zhang, and R. T. Weitz, Quantum cascade of correlated phases in trigonally warped bilayer graphene, Nature (London) **608**, 298 (2022).

[47] T. Han, Z. Lu, G. Scuri, J. Sung, J. Wang, T. Han, K. Watanabe, T. Taniguchi, H. Park, and L. Ju, Correlated insulator and chern insulators in pentalayer rhombohedral stacked graphene, arXiv:2305.03151.

[48] Y. Jang, Y. Park, J. Jung, and H. Min, Chirality and correlations in the spontaneous spin-valley polarization of rhombohedral multilayer graphene, Phys. Rev. B **108**, L041101 (2023).

[49] M. Das and C. Huang, Unconventional metallic magnetism: Non-analyticity and sign-changing behavior of orbital magnetization in abc trilayer graphene, arXiv:2308.01996.

[50] Y. Zhang, N. F. Q. Yuan, and L. Fu, Moiré quantum chemistry: Charge transfer in transition metal dichalcogenide superlattices, Phys. Rev. B **102**, 201115 (2020).

[51] Y. Zhang, T. Liu, and L. Fu, Electronic structures, charge transfer, and charge order in twisted transition metal dichalcogenide bilayers, Phys. Rev. B **103**, 155142 (2021).